Journal of Photochemistry & Photobiology, A: Chemistry 441 (2023) 114692

Contents lists available at ScienceDirect

Journal of Photochemistry & Photobiology, A: Chemistry

journal homepage: www.elsevier.com/locate/jphotochem

# Surface engineering of $Bi_2MoO_6$ as an efficient photoanode in tandem water splitting system by pulsed sonoelectrodeposition

Mahboobeh Zargazi [a], Mohammad H. Entezari [a,b,*]

[a] Sonochemical Research Center and Environmental Chemistry Research Center, Department of Chemistry, Faculty of Science, Ferdowsi University of Mashhad, Mashhad, Iran

[b] Environmental Chemistry Research Center, Department of Chemistry, Faculty of Science, Ferdowsi University of Mashhad, Mashhad, Iran

ARTICLE INFO

*Keywords:*
Bismuth molybdate
Sonoelectrodeposition
Photoelectrochemical
Crystal facet
Oxygen vacancy

ABSTRACT

The systematic and controlled synthesis of surface vacancies in semiconductors consider as a promising rout to modify their properties. Therefore, synthetic methods that can create these surface defects in nanomaterials are of great interest. Bismuth molybdate with engineered surface defect growing on its different crystal faces can be an excellent candidate for photoelectrochemical (PEC) water splitting. Simultaneously engineering the growth of the desired crystal face and creating surface vacancies on it would be very difficult. Herein, sonoelectrodeposition (SED) applied with continuous and pulse modes. The two different modes of ultrasound led to create two unexpectedly morphologies with different exposed crystal facets. Pulsed sonoelectrodeposition (PSED) method caused raspberry-like morphology with {0 1 0} desired exposed facet including high amounts of stabilized Oxygen vacancies (OVs). High efficiencies of PEC and dye sensitized solar cell (DSSC)/PEC with prepared photoanode originated from high amount of stabilized OVs, different exposed crystal facets and morphologies. The solar to hydrogen (STH) conversion in unassisted water splitting system (DSSC)/PEC was about 3.62%. Results confirmed that pulse mode of ultrasound acts as a proper method for simultaneously engineering of desired facet growth and creation of high amount of stabilized OVs on its surface.

## 1. Introduction

In recent years, the majority of researchers have focused on the semiconductor synthesis with defined morphologies, which originate from tailoring the exposed facets [1,2]. Surface engineering of photocatalysts at the nanoscale is done by changing the synthesis conditions such as using a surfactant, changing temperature, or applying combination methods. Different exposed crystal facets also give a promising fortunate for making of surface vacancy, which has a brilliant effect on photocatalytic performance [3,4].

Nowadays, surface oxygen vacancies (OVs) play a key role in the photocatalytic efficiency of semiconductors [5,6]. OVs provides active sites for charge regulating and changing optical feature of photocatalyst, let to tune the band structure of the semiconductor. The photoresponse region of semiconductors extended to visible or near-infrared regions by introducing OVs through the structure of the photocatalyst materials. It is well-known that the interfacial space of the semiconductors usually has a crucial role in the band structure and stability of created OVs. Generation of localized OVs on the different exposed facets of semiconductors exhibited excellent results, which imply to the importance of these topics. Bismuth-based photocatalysts such as $BiVO_4$, BiOCl, and $Bi_2MO_6$ (M = W or Mo) are very noticeable due to layered structures, narrow band gaps, and tailoring of crystal facets, which have shown high photocatalytic performances in environmental remediation and energy storage [7–9]. There is an appropriate relation between photocatalytic efficiency and crystal facets of Bi-compounds [10–12]. For instance, {0 1 0} crystal facet of $BiVO_4$ has been exhibited higher photocatalytic oxygen evolution than {1 1 0} facet notwithstanding {1 1 0} facets have been shown the oxidation functional facet compared to {0 1 0} facet [13]. An eye-catching semiconductor of aurivillius triplet-oxides categories is bismuth molybdate ($Bi_2MoO_6$) which can have variable valence band (VB) positions due to different exposed crystal facets or the presence of OVs on these facets [14]. Recently researches have extensively demonstrated that the exposed facets of $Bi_2MoO_6$ have an obvious effect on their photoelectrocatalytic and photocatalytic activities [15]. For photocatalytic degradation of pollutants, Long and co-

* Corresponding author at: Sonochemical Research Center and Environmental Chemistry Research Center, Department of Chemistry, Faculty of Science, Ferdowsi University of Mashhad, Mashhad, Iran.

*E-mail addresses:* moh_entezari@yahoo.com, entezari@um.ac.ir (M.H. Entezari).

https://doi.org/10.1016/j.jphotochem.2023.114692
Received 27 December 2022; Received in revised form 18 February 2023; Accepted 13 March 2023
Available online 17 March 2023

workers [16] illustrated that the dominant {0 1 0} facet of $Bi_2MoO_6$ (BMO) nanobelts had been shown higher photocatalytic efficiency compared to other facets. Indeed, the oriented {0 1 0} facet of BMO has offered active oxidation sites for the production of highly active oxygen species. On the other hand, a few studies have been conducted on the influence of exposed crystal facet on photocatalytic water oxidation by BMO [8,17,18] due to complexity and unknown topic.

Active crystal facets for BMO are {0 1 0}, {0 0 1}, and {1 0 0}, which suggested different photoelectrochemical performances due to differences in energy levels and oxidative or reductive properties. It was obvious that water oxidation process is rarely a determining step in overall water splitting because oxidation reaction needs four electrons while reduction reaction needs two electrons. BMO nanostructures have intrinsic and imposed OVs on their crystal facets that led to excellent photocatalytic performances. OVs can enhance the charge density, conductivity, and facilitate photogenerated charge transport due to upshift the fermi level in the BMO conduction band (CB) [19]. Photoinduced holes could be transferred from bulk to surface by these OVs too. Intrinsic OVs are on the {0 1 0} crystal facet, which originated from $Bi_2O_2^+$ layers, but this sort of OVs is minimal. Theoretical analyzes have predicted the existence possibility of two sites for formation of OVs on the different exposed facets of BMO [15]. The creation of localized OVs on the exposed crystal facet {0 1 0} is very hard due to the presence of energy barriers. In contrast, the creation of OVs on the {0 0 1} or {1 0 0} facets is an easier strategy. Commonly, OVs have been constructed in the nanostructures by complex conditions such as high reductive environments or under the high temperatures of calcination with explosive gas purging. Therefore, the control and creative formation of OVs on the selectively exposed facets with mild conditions has been the limelight recently.

The main challenge of BMO films is their low stability from the view of stickiness as photoelectrode in water splitting systems. Previous research indicated 2D or 3D nanostructures such as nanoplates or microspheres had higher stickiness than 1D structures such as nanorods and nanobelts [8]. On the other hand, 2D or 3D morphologies can be applied for overcoming the rapid recombination and slow migration of photogenerated charges of pristine BMO [14]. To end, according to the mentioned topics, it can be claimed that the engineering of new morphologies with stable OVs is the most challenging aspect in the preparation of BMO photoelectrodes [20]. Photoelectrochemical (PEC) water splitting needs to biased external potential to hydrogen evolution because of the intrinsic electronic structure of photoelectrode materials [21,22]. To achieve unassisted solar water splitting, PEC systems were coupled with photovoltaic (PV) cells to fabricate self-biased PEC/PV system. In the recent years, a few studies have been carried out to combine of dye-sensitized solar cell (DSSC) with PEC systems due to the low efficiency and instability of DSSC cells [23,24]. On the other hand, this solar cell is the simplest and cost-effective cell with enough photovoltage to run water splitting without external potentials. Recently, a few reports presented that they have demonstrated high solar to hydrogen (STH) conversion efficiency for PEC/DSSC tandem systems [25]. For example, Shi et al. [24] could gain STH efficiency of about 5.7% with $WO_3$/W- $BiVO_4$ photoelectrode as photoanode of PEC system.

Herein, highly stable 2D and 3D morphologies of BMO with different stable OVs can be fabricated by sonoelectrochemical methods in two continuous and pulse modes. New morphologies obtained from the growth of different crystal facets under synthesis conditions. 3D raspberry-like BMO were synthesized with OV-rich nano-bricks on the {0 1 0} exposed crystal facet, while 2D plate-like BMOs were synthesized with OV-rich on the oriented {1 0 0} crystal facet. Pulse synthesis method not only led to formation of controlled active OVs on the {0 1 0} crystal facet but also caused enhancement of stability of OVs (Bi-O). Highly efficient STH conversion of 3.62% obtained from DSSC/PEC systems with PSED samples.

## 2. Experimental section

All chemicals supplied by Merck, Sigma Aldrich and used without further purifications.

### 2.1. Preparation of $Bi_2MoO_6$ films with different morphologies

Typically, the electrolyte was formed from 5 mmol $Bi(NO_3)_3{\cdot}5H_2O$, 5 mmol $Na_2MoO_4{\cdot}2H_2O$, and 5 mmol $Na_2EDTA$. FTO glass ($2 \times 1$ $cm^2$-Sharif Solar Company-Iran) used as a working electrode in a 3-electrode electrochemical setup (SAMA 500, Iran). The sonoelectrodeposition method was employed in two modes, one pulse (PSED) and another in continuous situation (SED). The SED method was carried out under constant current (3 mA), at 70 ∘C for 30 min under continuous sonication (Horn- BRANSON, digital Sonifier 450, and 20 kHz) with 40% sonication amplitude. PSED method was similar to SED except with pulse sonication ($t_{on} = 1$ sec and $t_{off} = 2$ sec). Preparation methods are depicted in Scheme 1 with more details.

### 2.2. Characterization of BMO films

The synthesized films were examined by X-ray diffraction (XRD, Explorer GNR-Italia) to determine the crystallite structure and phase. Functional groups of samples were detected by Fourier transform infrared spectroscopy (FT-IR, AVATAR 370-USA). Raman spectra of the films have been recorded with AVANTES-Poland. The morphologies of the films were observed using both Field emission scanning electron microscopy (FESEM-MIRA3 TSCAN) and transmittance electron microscopy (TEM, EM-Philips BioTwinCM12). High-resolution TEM (HRTEM, TEC9G20-USA) was used to identify of crystal facet and OVs. The diffuse reflectance spectrum (DRS) of prepared films was examined using an UV–vis spectrophotometer (LABOMED 2950). Destiny of photoinduced charges was determined by photoluminescence emission spectra (PL, Perkin Elmer LS45). The thickness and surface of films were studied by atomic force microscopy (AFM) with ARA Research-Iran. OVs and chemical states were evaluated by X-ray photoelectron spectra (XPS) with AvaSpec − ULS − TEC, Poland.

### 2.3. Photoelectrochemical study

The obtained films were applied as photoelectrode in a 3-electrode electrochemical set up (SAMA-500, Iran). The synthesized films, Pt plate, and Ag/AgCl were used as the working, counter, and reference electrodes, respectively. The applied electrolyte for photoelectrochemical evaluation is 0.5 M $Na_2SO_4$. Linear sweep voltammetry (LSV) was recorded to estimate the resulted photocurrents from prepared photoelectrodes under light irradiation (AM 1.5G) by solar simulator system (SS-104, NTN Arvin Company) with Xe-lamp (Osram-150 W). Electrochemical impedance (EIS) study was conducted by Auto lab (302n-Poland) under light illumination.

Photocurrent-potential and photocurrent-time curves were recorded under simulated sunlight, generated by a solar simulator with an air mass 1.5 G filter. The light intensity of the solar simulator was calibrated to 1 sun (100 mW/$cm^2$). The amounts of evolved $H_2$ and $O_2$ were measured at defined time using Gas chromatography (Agilent 7890A-USA) with a 5 Å molecular sieve column.

Incident photon conversion efficiency (IPCE) was evaluated under Xe-lamp (Osram-150 W) with a cut-off UV region. IPCE values were calculated by Eq. (1):

$$IPCE(\lambda) = \frac{J_{ph} \times 1240}{P_{light} \times \lambda} \quad (1)$$

where λ and $P_{light}$ are the incident light wavelength (nm) and the light power intensity, respectively.

ABPE was determined from the photocurrent-potential curve by Eq.


**Scheme 1.** Schematic of preparation methods for BMO films.

(2):

$$ABPE = \frac{J_{ph} \times (1.23 - V_{bias})}{P} \quad (2)$$

To determine the flat band position and carrier numbers, Mott-Schottky analysis (by Auto lab, 302n-Poland) was done at potential range of −0.7 to 0.0 vs. Ag/AgCl with AC frequency 10 kHz under light illumination.

### 2.4. Synthesis of dye-sensitized solar cell (DSSC) and tandem cell

DSSC prepared by the following steps. First, cleaned FTO was pre-treated by $TiCL_4$ (40 mM, Merck) solution for 0.5 h at 70 °C and then rinsed with ethanol and deionized water. Nanocrystalline $TiO_2$ paste (20 nm) was deposited on treated FTO substrate by a doctor blade method and it was heated at 500 °C for 0.5 h. Next step, $TiO_2$ anatase paste (300 nm) as the scattering layer was deposited by the doctor blade printing and it was sintered at 500 °C for 0.5 h. The prepared films were treated by $TiCl_4$ solution according to the first pretreatment. Afterward, the films were immersed in N179 dye solution for 20 h and then the non-attached dyes were removed by dipping in ethylacetate solution for ten min. To fabricate the cathode, Pt paste was deposited on the FTO substrate by doctor blade printing and it was sintered in maffle furnace for 0.5 h. The prepared photoanode (dye-sensitized $TiO_2$) and Pt cathode were connected together by a 50-mm surlyn polymer. The electrolyte ($I^-/I_3^-$) was injected into the sandwiched cell from a hole drilled on the Pt cathode and the hole was sealed by surlyn polymer. The prepared DSSC was shown an open circuit voltage ($V_{OC}$) about 0.97 V and short-circuit current density ($J_{SC}$) 8.7 mA $cm^{-2}$ (see Fig. 2Sa (supporting file)). IPCE (see Fig. 2Sb (supporting file)) demonstrated the quantum capability of DSSC in 480 nm wavelength, which confirmed a good response for light capturing of the visible region. Proposed configurations for placing two cells (PEC and DSSC) are shown in Fig. 3S (supporting file).

## 3. Results and discussion

### 3.1. Fabrication and characterization of the plate and strawberry-like of BMO

Applying SED and PSED methods led to various morphologies with special crystal's orientation. SED method constructs BMO films with flower like which are self-assembled from the plate-like structures while, raspberry-like morphology obtained from the PSED approach. Indeed, these morphologies originated from the creation of the preferred orientation of different crystal facets. XRD patterns for both films are shown in Fig. 1a and demonstrate different intensities for crystal planes. BMO prepared from the SED method shows higher intensity compared to the sample prepared from the PSED method. A little shift to large angels for the PSED sample compared to the SED sample is assigned to the presence of OVs. Defects in the crystal lattice create disorder and strain, which causes the peak to shift or change its intensity. Other works also demonstrated a slight shift of XRD pattern can be assigned to the mount of OVs [19,26]. FTIR spectra for both samples are indicated in Fig. 1b and show the corresponded peaks of Bi-O and Mo-O functional groups. The peaks in around 400 and 950 $cm^{-1}$ assigned to Bi-O and Mo-O bands, respectively [27]. The inset figure in Fig. 1b shows that Bi-O and Mo-O peaks have slight displacements. These displacements in FTIR spectra could be assigned to the presence of different OVs in BMO nanostructures [28]. Peaks in 585 and 612 $cm^{-1}$ were indexed to Bi-O bonds and their shifts mean deformation of Bi-O bonds. The absorption peaks at 848 and 947 $cm^{-1}$ were assigned to Mo-O bonds in $MoO_6$ octahedral. The Raman spectra of BMO films were depicted in Fig. 1c and the results confirmed the presence of Bi-O and Mo-O groups for both samples. The low intensity of peaks for the PSED sample suggested that Mo-O and Bi-O bonds have disordered in comparison to the SED sample. The peaks appeared in 254 and 320 $cm^{-1}$ are indexed to symmetric and asymmetric deformational motions of Mo-O bonds. Peaks in the range of 600–810 $cm^{-1}$ were attributed to the stretching vibrations of Mo-O

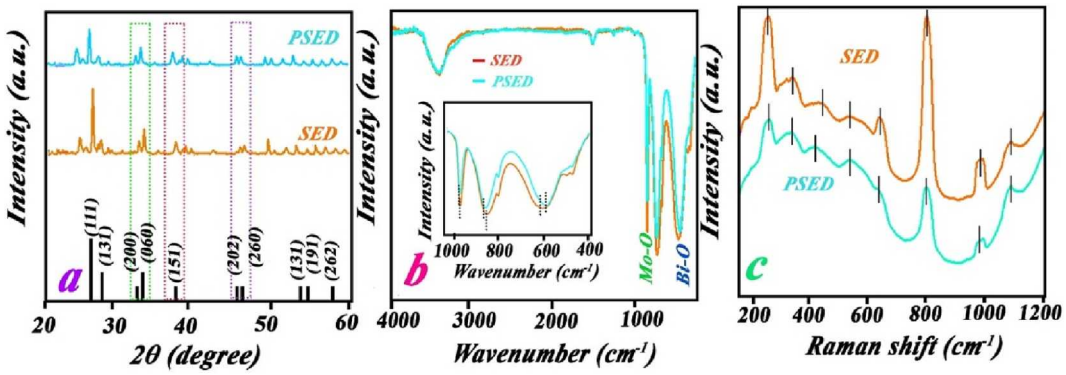


**Fig. 1.** (a) XRD pattern, (b) FTIR spectra, and (c) Raman spectra for BMO synthesized by SED and PSED approaches.

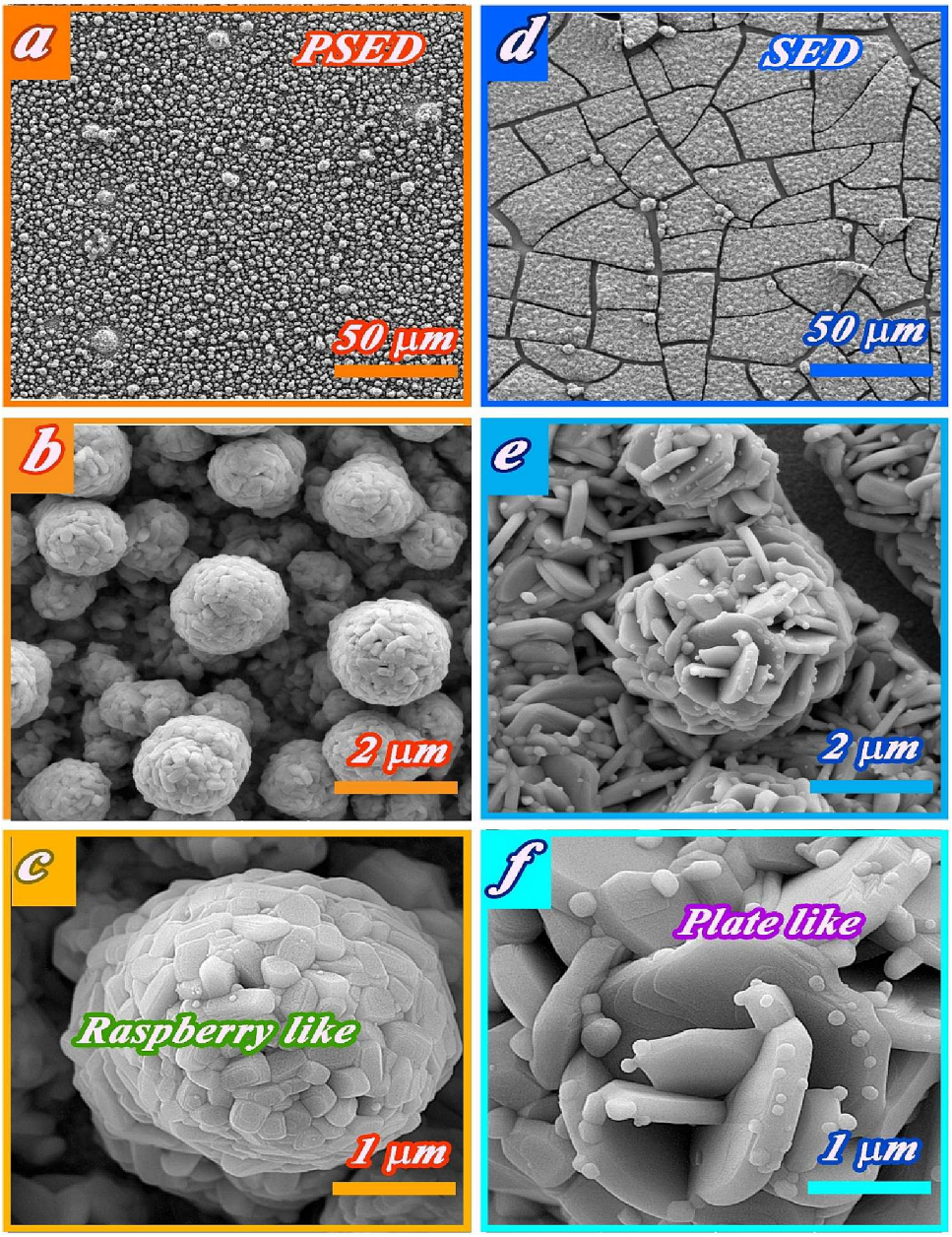


**Fig. 2.** SEM profiles for PSED (a-c) and SED (d-f) films.

octahedrons, which refers to the motion of apical oxygen atoms [29]. The apical oxygen atoms orient to $(Bi_2O_2)^{2+}$ layers. Peak at 630 $cm^{-1}$ was related to the stretching of octahedrons, but it has not appeared for the PSED samples [30]. Numerous OVs in the PSED sample caused to deform BMO structure that is assigned to the low intensity of Raman peaks (Fig. 1c). Other studies suggested the absence of oxygen atoms in Bi-O or Mo-O bonding besides the growth of different facets led to decrease of Raman intensities [17,31,32].

Raspberry-like structure of the PSED sample was indicated by SEM profiles with different magnifications, which are shown in Fig. 2a-c. It is clearly observed that small nano bricks were produced under pulse conditions, self-assembled together for the creation of raspberry-like morphology. The size of these nano bricks almost is 160–180 nm. This morphology was designed by engineering the selective crystal facets of BMO under pulse condition. The resulted morphology was originated from more growth of crystal facet in {0 1 0} direction than other directions ({0 0 1} or {1 0 0}). While the SED method (see Fig. d-f) could produce plate-like BMO structures due to continuous sonication and growth crystal facets of {1 0 0} but kind of arrangement led to the appearance of exposed crystal facets {0 1 0} and {1 0 0} simultaneously. Togetherness of two crystal facets originated from continuous acoustic streaming that the nanoplates can only self-assembled together to create flower-like shapes. Indeed, continuous sonication led to the form of self-assembled nanoplates but in case of pulse sonication at off time, plate growth is stopped and could be oriented to form a spherical shape. On the other hand, brick-like structure in the PSED method grown and has a chance for rotation to assemble nano-bricks and form raspberry-like morphology. Films prepared by the PSED method are homogenous and crack-free in their structure (comparison Fig. 2a and 2d). Continuous sonication led to creation of cracks in the SED sample due to destruction power of high-intensity ultrasound. Longitudinal sizes of plates are about 600–1500 nm, but plate thickness is almost 300 nm. It is noteworthy that in our previous work, nano coral-like BMO films were fabricated in the absence of ultrasonic waves [8] which preferred exposed facet is {0 1 0}.

The corresponding TEM images in Fig. 3a, b indicated raspberry and

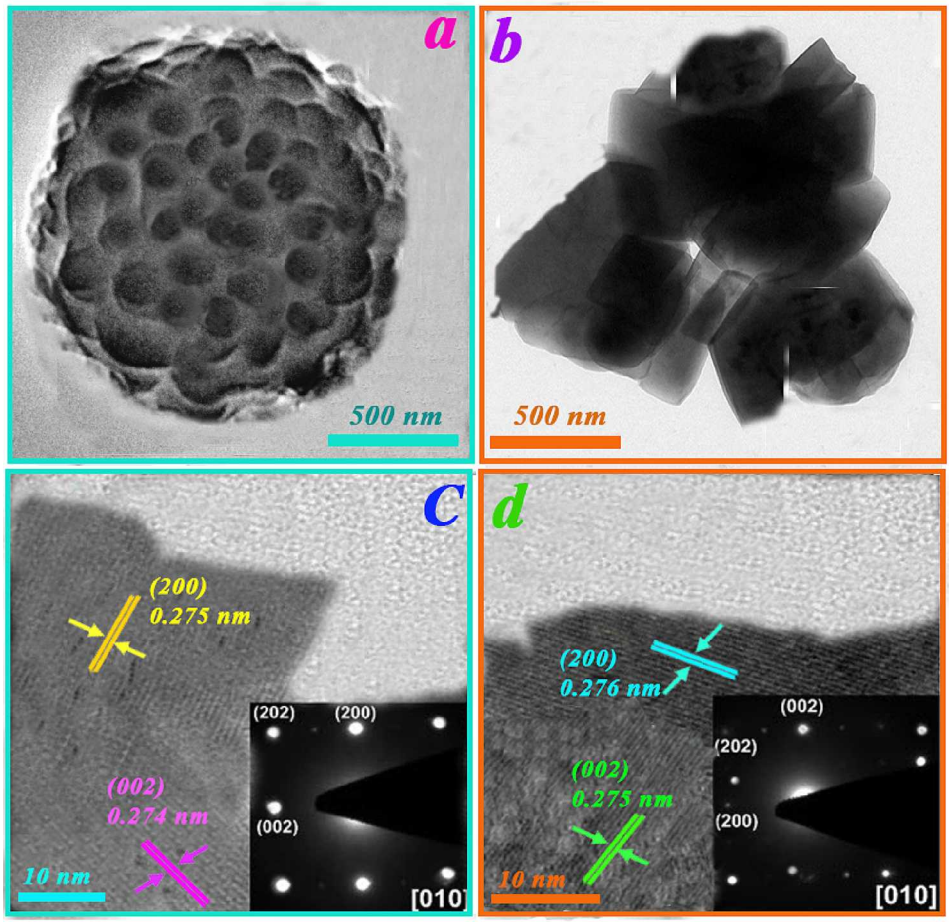


**Fig. 3.** TEM profiles for (a) PSED and (b) SED and the corresponded HRTEM images and SAED patterns (inset figures) for (c) PSED and (d) SED.

plate-like morphologies for PSED and SED samples, respectively. HRTEM images of these samples were demonstrated in Fig. 3c, d, which prove the presence of (200) and (002) crystal planes. HRTEM image of PSED film in Fig. 3c shows the planar spacing 0.274 nm and 0.275 nm for (002) and (200) crystal planes of orthorhombic BMO, respectively. This suggested the preferred crystal growth and assembled to form 3D structures. The single crystal structure of the prepared BMO films was confirmed by SEAD patterns with inset figures in Fig. 3c, d. According to XRD and HRTEM results, exposed crystal facets for BMO plates are {100} and {010} facets.

According to proposed geometric models for BMO, {010} facet included numerous O-atoms which resided in the valence band of BMO. OVs not only act as trapping sites for charge carriers, but also introduce as photoactive sites for water oxidation. The number of OVs in the PSED sample is significantly higher than the SED sample, which led to the deformation of its structure based on Raman spectra and XRD patterns.

AFM images of SED film in Fig. 4Sa-c (Supporting File) shows the overlapped plates in various AFM modes. The 3D AFM image has also confirmed the presence of plates and the film thickness is 541.8 nm. The amplitude mode of AFM image for the SED sample (see Fig. 4Sc) indicates the oriented plates and the formation of flower-like structures. In contrast, the PSED method can form raspberry-like shapes, assembled from nano-bricks (see Fig. 4Sd). The 3D AMF image in Fig. 4e confirms the presence of nano-bricks and the film thickness is 767.1 nm. The Amplitude mode of the AFM image in Fig. 4Sf was also indicated assembled nano-bricks of BMO. More thickness of the PSED film could attribute to the formation of raspberry morphologies. Furthermore, formation of plate-like morphology was assigned to continuous sonication which it dissolves dendrite like structures and led to grow in specific facet.

More details about the surface chemistry of the prepared plate and raspberry-like BMO films were investigated by X-ray photoelectron spectroscopy (XPS). Bi orbitals in both samples are shown in Fig. 4a and a small displacement was observed at peak locations due to the presence of OVs [29]. Mo orbitals were also appeared in corresponding wavelengths and show some shifts (about 0.2 eV) to lower binding energies for the PSED samples (Fig. 4b). Broaden peak for O 1 s orbitals is shown in Fig. 4c, which includes Bi-O and Mo-O bonds for BMO samples [29,30]. The high intensity of the Bi-O peak is clearly observed for the SED sample, which indicates the high density of oxygen atoms in the preferred facets. However, the lower intensity of the Bi-O bond for the PSED sample indicated the absence of O atoms on the related exposed facets. Peaks of Mo-O bond for SED and PSED samples have different intensities which assigned to the presence of OVs in Mo-O bonding [30,33]. The presence of OVs in both of samples was determined by ESR analysis (Fig. 4d). As expected OVs signals were appeared with different intensities at $g = 2.001$ and $g = 2.000$ for PSED and SED samples, respectively. [34].

The optical properties of samples are an essential factor for the evaluation of their photocatalytic performance. Hence, DRS spectra for both films are depicted in Fig. 5a. The light absorption of photocatalytic films confirmed that the PSED sample had a higher absorption in the visible region than the SED film. Band gap of BMO films was calculated from the Tauc equation and the results were inserted in Fig. 5b. The PSED sample has a lower band gap (2.33 eV) in comparison with the SED (2.40 eV). These results are consistent with UV–visible spectra.

Light-harvesting efficiencies (LHE) of samples are the main parameter for the investigation of light capturing. High LHE indicates that

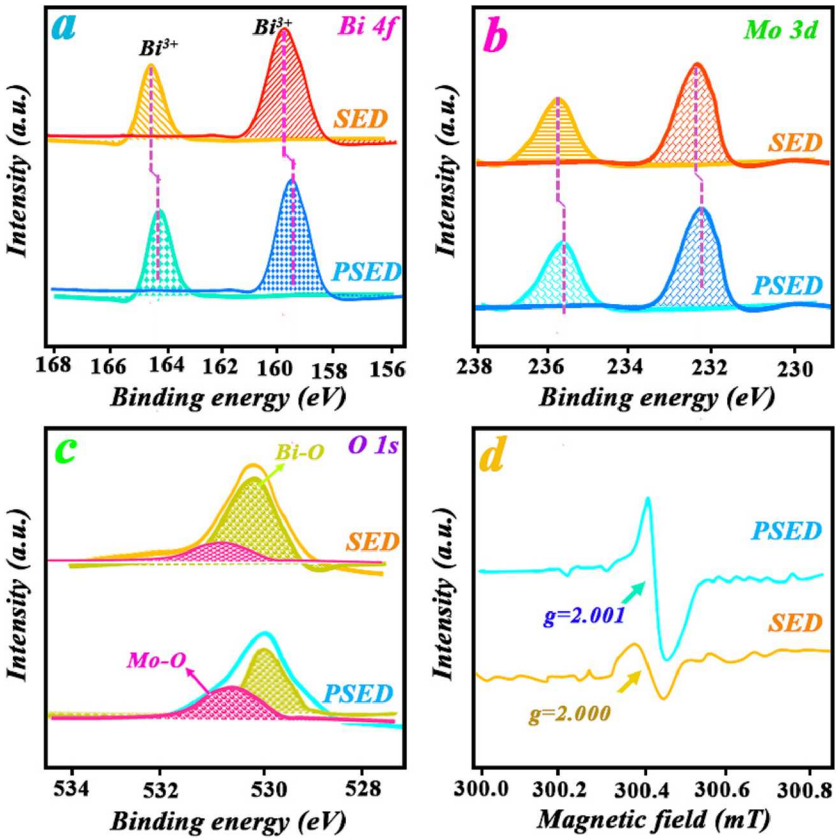


**Fig. 4.** XPS patterns of (a) Bi, (b) Mo, (c) O, and (d) ESR spectra for SED and PSED.

BMO film could have more trapping sunlight energy as a renewable source. The BMO synthesized by PSED with raspberry morphology demonstrated higher LHE than SED with flower-like morphology as shown in Fig. 5c. The discrepancy of LHE is observed in the range of 400–800 nm that is attributed to the presence of OVs in the nanostructures. PL spectra can determine the fate of photo-generated charge carriers by BMO films. As observed in Fig. 5d, the PSED sample indicated a shift for PL peak compared with the SED sample, which suggested the presence of different OVs in their structures. Charge separation efficiency ($\eta_c$) and charge injection efficiency ($\eta_{in}$) are crucial factors in PEC performance. High LHE in Fig. 5c confirmed the high photoabsorption ability ($_{Jabs}$) of photoelectrodes [35]. Therefore, increase of separation and injection efficiencies (Fig. 5e and f) led to improve the PEC efficiency. PSED sample shown higher surface transfer and bulk transport than the SED sample. This can be attributed to the different exposed facet {0 1 0} and high stable OVs in this sample.

### 3.2. PEC response

Open circuit potential (OCP) is an effective analysis for the determination of produced voltage under light irradiation by BMO films. Based on Fig. 6a, the resultant photovoltage of the PSED sample is higher than the SED sample due to a negative shift to higher potentials. Photovoltages from PSED and SED samples are 380 and 180 mV, respectively. The recombination rate of charge carriers was also evaluated by the OCP curve slop after light illumination and in the dark. Low slop was referred to low rate of charge recombination, which both of samples shows low recombination rate. Obtained photocurrent from both BMO films was observed in Fig. 6b by LSV curve. As can be seen in Fig. 6b, the PSED sample shows higher photocurrent than the SED sample, which can attribute to the high amount of OVs and active exposed crystal facet of {0 1 0}. The preferred exposed facet of PSED is {0 1 0}, while both of {0 1 0} and {1 0 0} facets of SED sample is exposed, simultaneously. Indeed, photogenerated electrons accumulated on {1 0 0} or {0 0 1} facets and photogenerated holes accumulated on {0 1 0} facet. It is noted that according to SEM, TEM, and AFM images, the preferred exposed facet for SED is {1 0 0}. Previous studies were indicating that {1 0 0} is a reductive facet of BMO [8,16]. Accumulation of photogenerated charge carriers on the different crystal facets led to high separation and prevented their recombination due to spatial separation. Exposed facet {1 0 0} for SED sample has more contribution in comparison with {0 1 0} facet, which can see from SEM and TEM images. It confirmed that the photogenerated holes are not available in comparison with PSED sample. According to the sizes of the nanostructures, high thickness of platelike SED sample led to reduction of charge diffusion and enhanced the recombination rate in comparison with nanosized bricks in the PSED sample. Onset potential for the PSED sample has a shift to negative potentials in comparison with the SED sample that suggested a high potential for water oxidation. Different OVs on {0 1 0} are more effective for PEC water splitting than those on {1 0 0} facet. OVs on the {0 1 0} can attribute to the shortage of oxygen atoms connected to Bi atoms, while OVs on the {1 0 0} can attribute to oxygen atoms connected to Mo atoms.

Chronoamperometry curves of samples under light and dark conditions were depicted in Fig. 6c. The obtained photocurrent from the PSED sample is higher than that of the SED sample, which is assigned to the various exposed facets for these samples. These results have been confirmed by other researchers and proved that the exposed facets play a key role in photoelectrochemical studies [15,27]. Fig. 6d showed that the photocurrent obtained from both samples under chopped illumination. It can be seen that the PSED sample showed a higher current compared to the SED sample due to its new kind of morphology.

EIS analysis of two films was studied under light illumination and results are presented in Fig. 7a. The Nyquist curve for the PSED sample has a smaller radius of semicircle than the SED sample. It can be attributed to high separation charge carriers for the film with exposed crystal facet ({0 1 0} with higher stable OVs amount in PSED sample. It

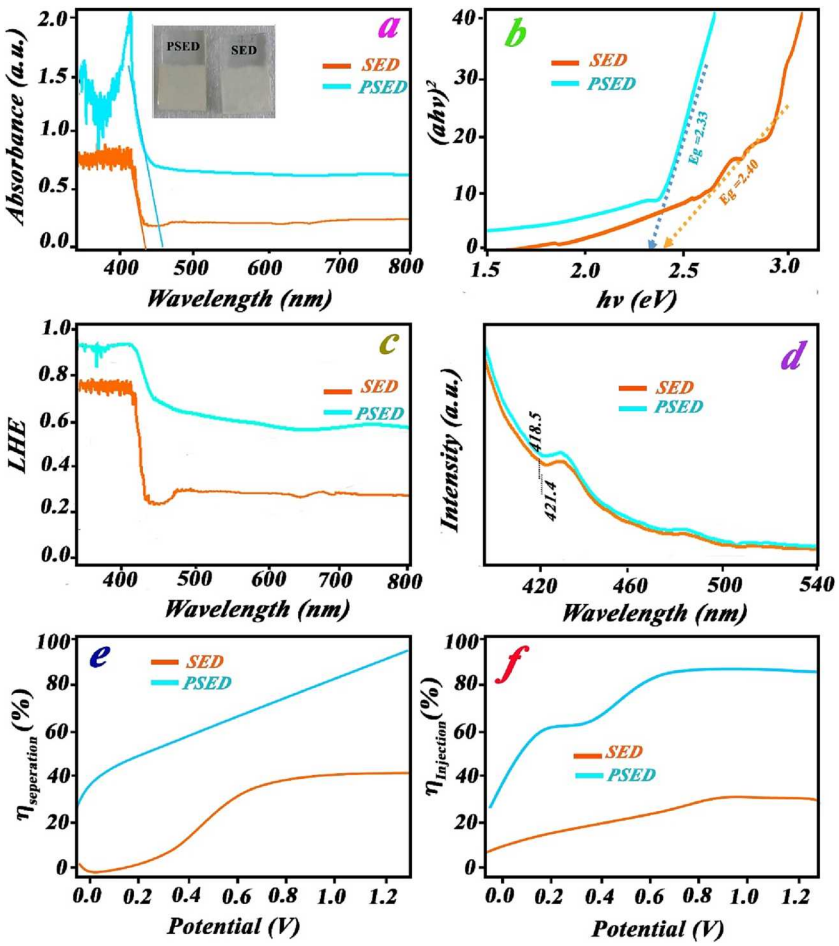


**Fig. 5.** (a) DRS-UV–vis spectra, (b) band gap calculation from the Tauc equation, (c) LHE, and (d) PL spectra, (e) charge separation efficiency vs. potential, and (f) charge injection efficiency vs. potential curve for PSED and SED films.

can be indicated high charge transferring for the PSED sample compared to the SED sample due to the presence of OVs and short routes in the PSED film. Lifetime of photogenerated electrons is known as a significant parameter for the evaluation of photocatalytic performance. Lifetime of photoinduced electrons calculated from the Bode plot. The maximum peak in the Bode plot according to the Eq. (3) has an inverse relation to the lifetime of electrons.

$$\tau = 1/2\pi f \tag{3}$$

where, τ and f are lifetime and frequency at maximum peak, respectively. Lifetime of photoinduced electrons from PSED and SED samples are 0.639 and 0.397 ms, respectively (see Fig. 7b). It indicates that the photogenerated electrons from the PSED sample have a longer lifetime due to the exposed crystal facet {0 1 0} and the presence of OVs on this facet and the effect of them in high separation photogenerated charge carriers. Fig. 7c shows Mott-Schottky plots for both samples. The PSED sample has lower slop compared with the SED sample, which confirmed the production of higher photoinduced charges by the PSED sample. The Flat band (FB) potential of the PSED sample is more negative than the SED sample, indicating a higher PSED potential for water oxidation [36]. Based on Fig. 7d, PSED and SED samples have ohmic contact with substrates and confirmed by symmetric and linear behavior of solid I-V curve. Herein, the presence of stable OVs on both samples resulted in an increase in semiconductor conductivity and this conductivity is also higher for the PSED sample.

In reality, holes and surface states manage the water oxidation process. Therefore, the holes are absorbed by the surface states and then they are transferred from the surface states to the water molecules at the interface (see Fig. 8a). To clarify the mechanism and kinetic of water oxidation, the investigation was conducted on the changes of resistances and capacitances of films that are attributed to the charge trapping and transferring at surface states and electrolyte interface. These parameters were determined from equivalent circuit (Fig. 8b) [37]. $C_{Bulk}$ infers to charge accumulation in the film bulk [38]. Higher capacity value ($C_{Bulk}$) for the PSED sample indicates the formation of more charge carriers (see Fig. 8c). On the other hand, reduction of $R_{trapping}$ (Fig. 8d) for the PSED sample expresses more restriction of charge (holes and electrons) trapping in surface states than SED sample. Increase of $C_{trap}$ (refers to charge accumulation at the surface sates) and decrease $R_{ct,trap}$ (attributes to the resistance of charge transferring from surface sates to electrolyte) (Fig. 8e, f) suggest effective charge transferring during PEC process. Others illustrated that conflict behavior between $C_{trap}$ and $R_{ct,trap}$ in the long run create higher photocurrents, which provided routs for charge transferring from surface states to electrolyte [38,39]. Decrease in $R_{ct,trap}$ vs. bias potentials in Fig. 8f refers to the photocurrent enhancement (compare to Fig. 6b). It is noteworthy that the PSED sample shows minimum resistance from 0.8 to 1.2 V (vs. Ag/AgCl), which justifies the high photocurrent in this range of bias potentials. These results confirmed that the PSED sample has more effective surface states than SED sample.

The ABPE values (Eq. (2) were measured for both samples from photocurrent density vs. potential data, the PSED sample reveals the maximum value of 1.22% at 0.213 V (vs. Ag/AgCl) (see Fig. 9a). IPCE values (Eq. (1) were measured for both samples under monochromatic light irradiation and results were demonstrated in Fig. 9b. It is remarkable that PSED sample shows higher IPCE value in the range of

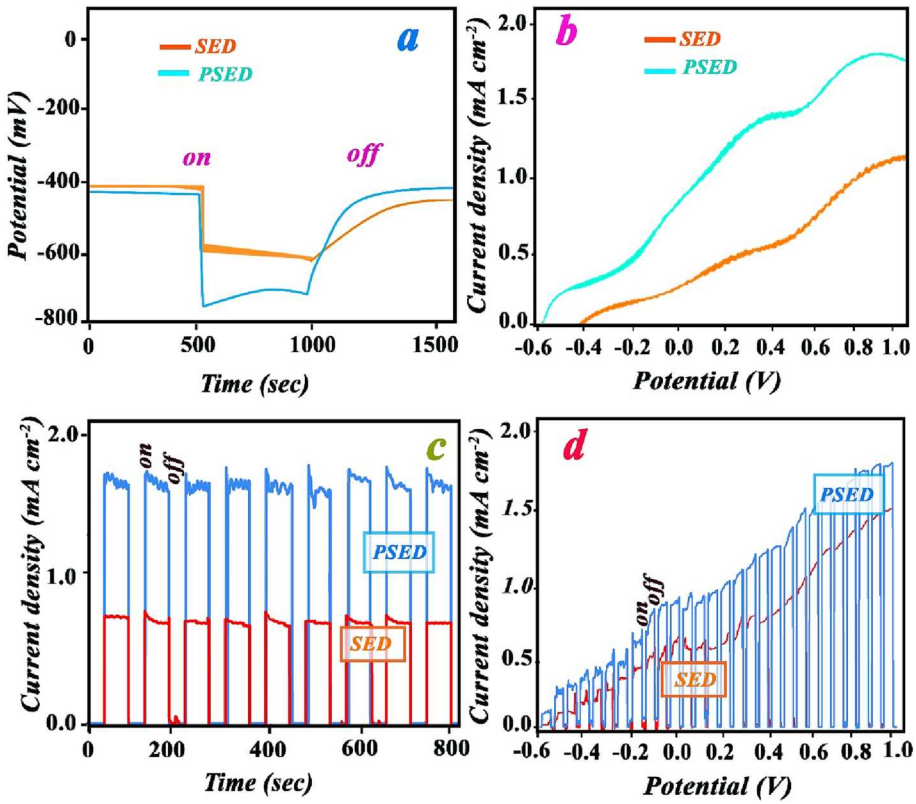


**Fig. 6.** Open circuit potential (a), photocurrent density -potential curve (b), current density-time curve (c), and photocurrent density- potential curve from chopped illumination for PSED and SED photoelectrodes in PEC system.

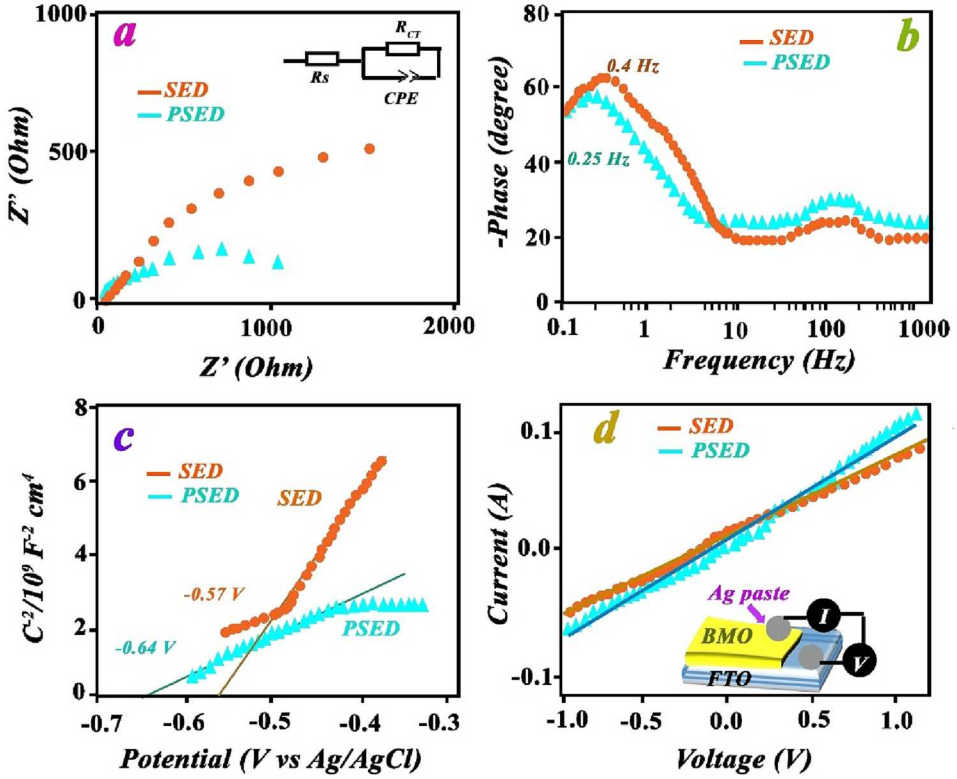


**Fig. 7.** Nyquist curve (a), Bode plot (b), Mott-Schottky curves (c), and solid-state I-V curve (d) for PSED and SED.

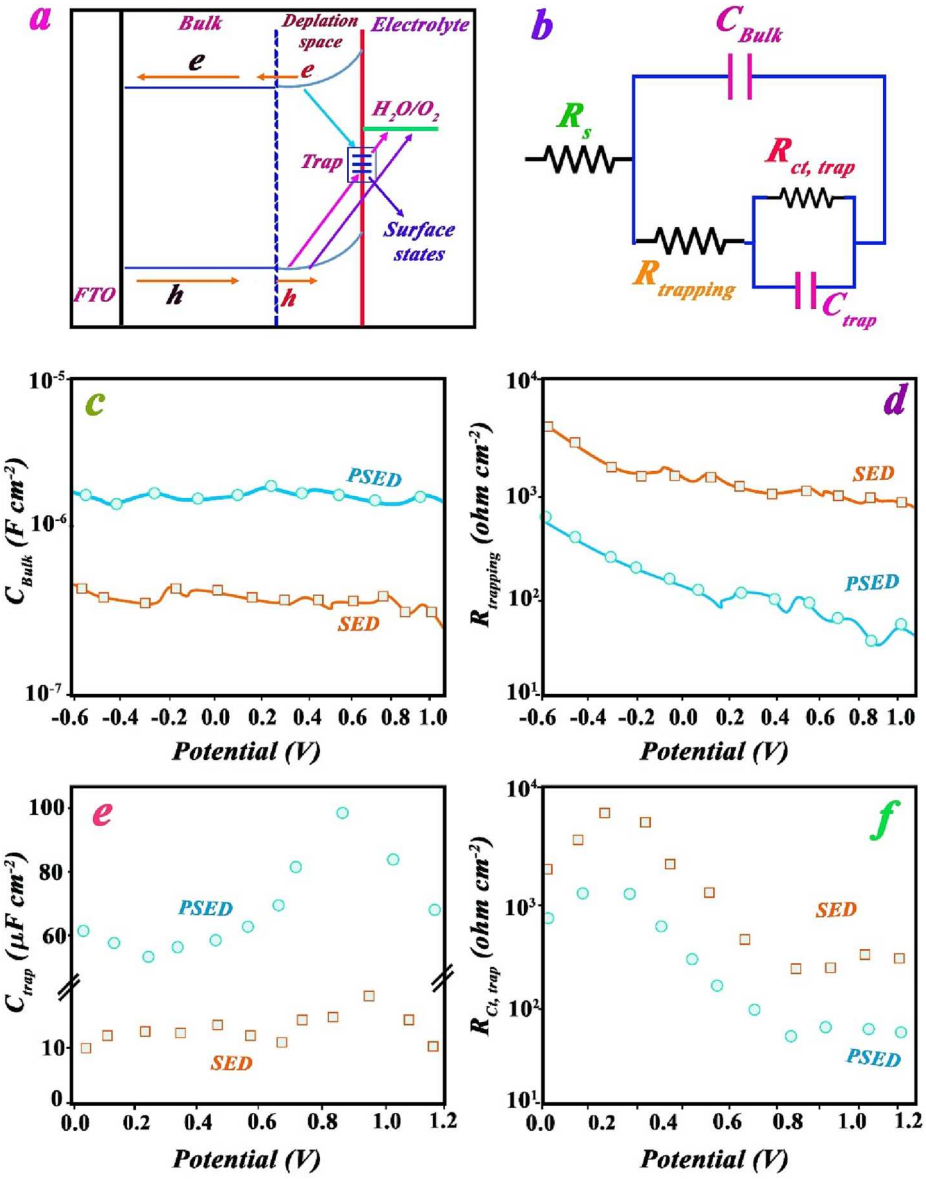


**Fig. 8.** (a) Physical model for charge dynamics in BMO electrodes/electrolyte interface, (b) corresponding equivalent circuit, resistance and capacitance elements related to charge trapping (c) $C_{bulk}$, (d) $R_{trapping}$, and charge transfer (e) $C_{trap}$, (f) $R_{ct,trap}$, of electrode/electrolyte interface under different bias potentials which are calculated from EIS spectra.

350–550 wavelength, which suggested higher adsorption ability of PSED sample than SED sample. To demonstrate the effect of vacancy states and exposed crystal facets on the separation efficiency of PSED sample, surface photovoltage (SPV) spectroscopy was employed (Fig. 9c). Positive behavior of SPV spectra was attributed to acceptor type of surface vacancies [40]. Large SPV for PSED sample implies to efficient separation of charge carriers, broaden peak was also created by Franz–Keldysh effect and shallow trap states [41]. Indeed, SPV spectra indicates the presence of trapping sites originated from surface vacancies.

Stability of produced photocurrent originated from photoelectrodes (J vs. time curve) can guarantee PEC performance. J-time plot (Fig. 9d) for prepared photoanodes through 10 h suggests long lifetime for photoelectrodes that reveals the stability of structure under applied potentials. The high stability of photoelectrodes also confirmed the high stability of structures and OVs. Furthermore, $H_2$ and $O_2$ evolution was evaluated and confirmed efficient PEC systems and the results indicated by Fig. 9d. The gas evolution rate for PSED sample was twice the SED sample.

### 3.3. PEC/DSSC tandem performance

The prepared DSSC as a photovoltaic cell was coupled with PEC in a tandem system. The synthesized BMO photoelectrodes were applied as photoanode in the PEC component of tandem PEC/DSSC. In this case, DSSC and BMO photoelectrodes applied in-situ two-electrode systems to measure current density-potential curves. Herein, low energy photons were absorbed by DSSC compartment due to the absorption of photons with high energies by photoanodes, which is consistent with the proposed configuration (Fig. 3S-supporting file). The photocurrent density-potential characteristics of the BMO photoelectrodes were investigated in a 0.5 M sodium sulfate solution (pH 6.8) under AM 1.5G illumination at the presence and absence of the DSSC (Fig. 10a). Operational photocurrent ($J_{OP}$) of the tandem system obtained from the intersection point of the curve of DSSC and photoanodes in PEC system (alone). Herein, operational currents are 2.95 and 2.03 mA for PSED and SED samples, respectively. The operational photocurrent from both tandem DSSC/PEC with synthesized photoelectrodes are indicated in Fig. 10b, which confirms the good stability and lifetime of these systems.

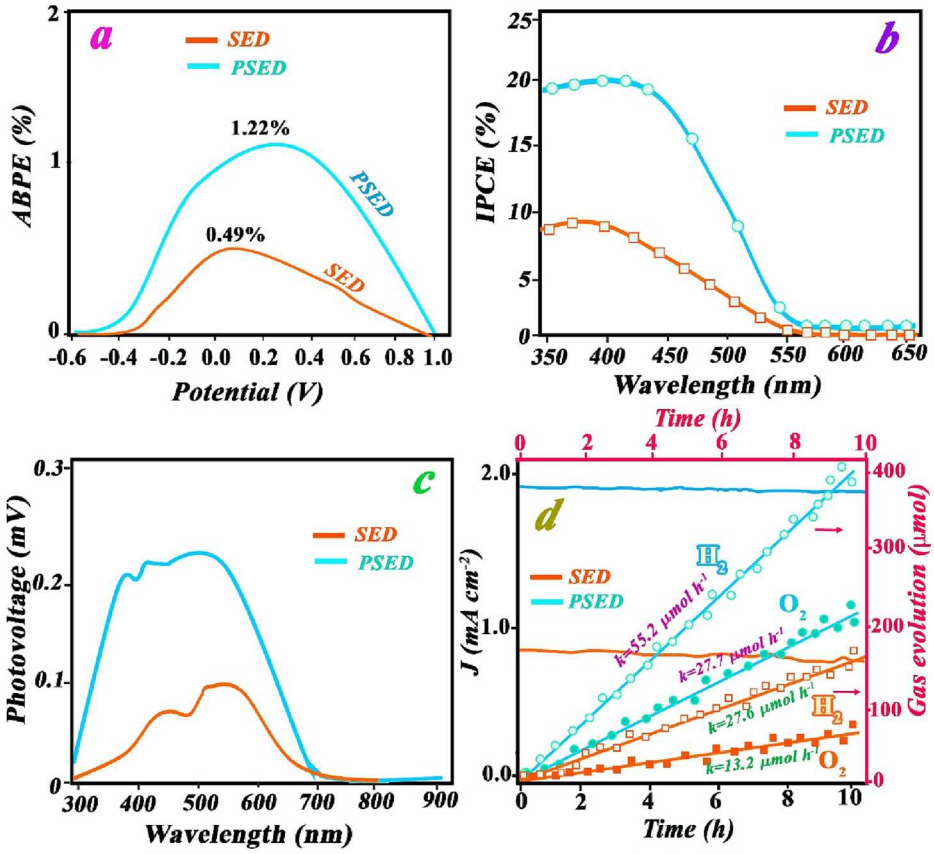


**Fig. 9.** (a) ABPE obtained from two electrodes cell in 0.5 M $Na_2SO_4$ under light illumination, (b) IPCE at 0.8 V vs. Ag/AgCl under monochromatic light illumination, (c) SPV spectra and (d) stability of prepared photoanodes (photocurrent density vs. bias potential) and evaluated experimental and theoretical $H_2$ and $O_2$ evolution.

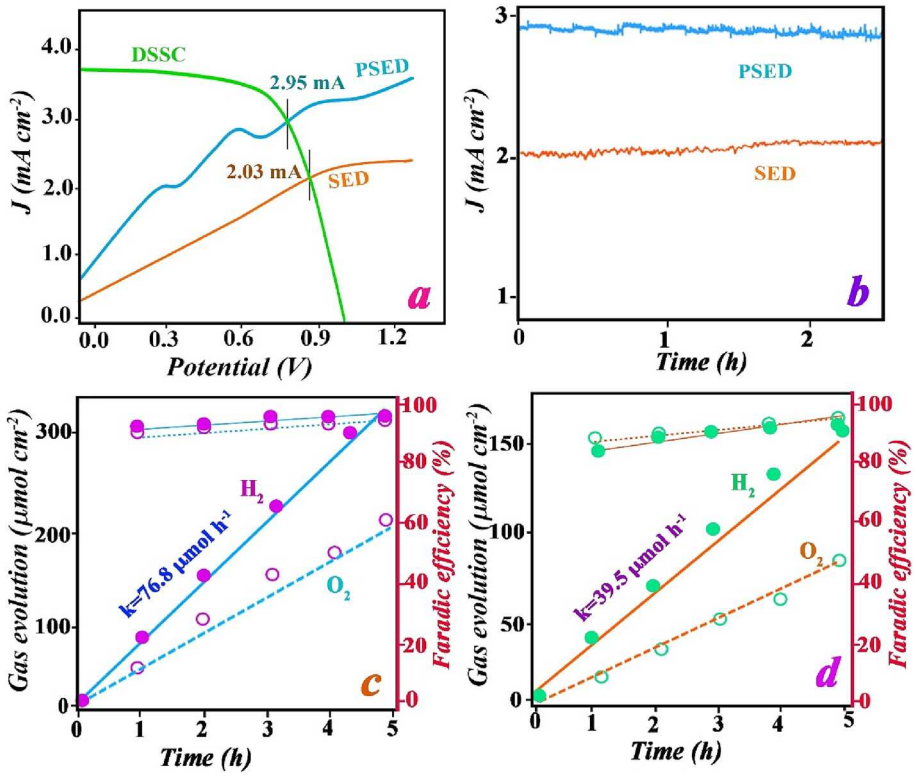


**Fig. 10.** Current density-potential curves of the DSSC and BMO photoelectrodes measured under 1sun (a), $J_{OP}$-time curves for DSSC/PEC tandem system with BMO photoelectrodes (b), gas evolution and Faradic efficiencies for tandem configuration with PSED (c) and SED (d) as photoanode.

Evolved gasses from tandem DSSC-PEC system were measured for both photoelectrodes without bias potential and the results are shown in Fig. 10c, d. In order to prevent gases cross over, the membrane was used and they collected from two district chambers. As expected, the amount of evolved gases in a tandem system with PSED photoelectrode is higher than another tandem system with SED photoanode. Faradic efficiencies for both tandem systems also indicated in Fig. 10c, d, which confirmed the almost good matching between experimental and theoretical (current density) evolution. STH efficiency of DSSC/PEC tandem was calculated from Eq. (4) due to faradic efficiencies near 100%.

$$\eta_{STH} = \frac{J_{op} \times 1.23}{P} \quad (4)$$

where, P is the power of irradiated light (100 $mWcm^{-2}$). According to resultant $J_{OP}$s from Fig. 9a, $\eta_{STH}$ obtained about 3.62% and 2.49% for tandem systems with PSED and SED photoanodes, respectively. These efficiencies are high for DSSC/PEC tandem systems with one external potential (DSSC) without any biased potential. The ratios of $H_2/O_2$ gases are 1.89 and 1.81 for tandem DSSC/PEC systems with PSED and SED photoanodes, respectively. These results suggested that the PSED photoelectrode is a proper photoanodes for tandem DSSC/PEC systems. Higher efficiency and stability of PSED sample were assigned to unique morphology and growth of exposed crystal facet {0 1 0} with controlled OVs.

## 4. Conclusion

To sum, two new morphologies with different growth of oriented crystal facets for BMO films were introduced by the combined method (sonoelectrochemical deposition). Pulse or continuous modes of sonication, has a vital role in the formation of new different morphologies. The PSED showed higher photocatalytic activity in the water oxidation process due to the growth of effective exposed {0 1 0} facets with a controlled amount of defect states. Proposed synthesis methods lead to fabricate highly stable BMO films with proper adhesion to substrate, in particular PSED. Herein, exposed crystal facets {0 1 0} have played in enhancing photo-generated carriers separating, which could increase PEC performance. The PSED sample has high surface, has an effective exposed facets with higher vacancy states than the SED photoelectrode. The prepared photoanodes used in tandem DSSC/PEC systems, were also indicated high photocatalytic performances for water oxidation. Unassisted water splitting systems (PEC/DSSC system) were demonstrated STH efficiency of 3.62 and 2.69 % for PSED and SED photoanodes, respectively. Finally, the sonoelectrochemical synthesis method can be considered as a new approach to simultaneously grow active exposed crystal facet and highly stable OVs, particular in pulse mode. Therefore, the PSED method is introduced for selective growth of crystal facets and the creation of surface defects in mild conditions.

## CRediT authorship contribution statement

**Mahboobeh Zargazi:** Writing – original draft, Visualization, Validation, Software, Investigation, Data curation. **Mohammad H. Entezari:** Writing – review & editing, Supervision, Methodology, Conceptualization.

## Declaration of Competing Interest

The authors declare that they have no known competing financial interests or personal relationships that could have appeared to influence the work reported in this paper.

## Data availability

Data will be made available on request.

## Acknowledgment

The support of Ferdowsi University of Mashhad (Research and Technology) is appreciated. We also acknowledge the central lab of Ferdowsi University of Mashhad.

## Appendix A. Supplementary data

Supplementary data to this article can be found online at https://doi.org/10.1016/j.jphotochem.2023.114692.

## References

[1] G. Liu, J.C. Yu, G.Q. Lu, H.-M. Cheng, Crystal facet engineering of semiconductor photocatalysts: motivations, advances and unique properties, Chem. Commun. 47 (24) (2011) 6763–6783.
[2] W. Tu, W. Guo, J. Hu, H. He, H. Li, Z. Li, W. Luo, Y. Zhou, Z. Zou, State-of-the-art advancements of crystal facet-exposed photocatalysts beyond TiO2: Design and dependent performance for solar energy conversion and environment applications, Mater. Today. 33 (2020) 75–86, https://doi.org/10.1016/j.mattod.2019.09.003.
[3] T. Butburee, P. Kotchasarn, P. Hirunsit, Z. Sun, Q. Tang, P. Khemthong, W. Sangkhun, W. Thongsuwan, P. Kumnorkaew, H. Wang, K. Faungnawakij, New understanding of crystal control and facet selectivity of titanium dioxide ruling photocatalytic performance, J. Mater. Chem. A. 7 (2019) 8156–8166, https://doi.org/10.1039/C8TA11475G.
[4] M. Li, E. Liu, H. Hu, S. Ouyang, H. Xu, D. Wang, Surfactant-free synthesis of single crystalline SnS 2 and effect of surface atomic structure on the photocatalytic property, Int. J. Photoenergy. 2014 (2014) 1–7, https://doi.org/10.1155/2014/394146.
[5] R. Fernández-Climent, S. Giménez, M. García-Tecedor, The role of oxygen vacancies in water splitting photoanodes, Sustain, Energy Fuels. 4 (2020) 5916–5926, https://doi.org/10.1039/D0SE01305F.
[6] X. Huang, X. Gao, Q. Xue, C. Wang, R. Zhang, Y. Gao, Z. Han, Impact of oxygen vacancies on TiO 2 charge carrier transfer for photoelectrochemical water splitting, Dalt. Trans. 49 (2020) 2184–2189, https://doi.org/10.1039/C9DT04374H.
[7] M. Zargazi, M.H. Entezari, Anodic electrophoretic deposition of Bi2WO6 thin film: high photocatalytic activity for degradation of a binary mixture, Appl. Catal. B Environ. 242 (2019) 507–517, https://doi.org/10.1016/j.apcatb.2018.09.093.
[8] M. Zargazi, M.H. Entezari, Ultrasound assisted deposition of highly stable self-assembled Bi2MoO6 nanoplates with selective crystal facet engineering as photoanode, Ultrason. Sonochem. 67 (2020), 105145-105154, https://doi.org/10.1016/j.ultsonch.2020.105145.
[9] M. Zargazi, M.H. Entezari, Sono-electrodeposition of novel bismuth sulfide films on the stainless steel mesh: Photocatalytic reduction of Cr (VI), J. Hazard. Mater. 384 (2020), 121300, https://doi.org/10.1016/j.jhazmat.2019.121300.
[10] Z. Yang, M. Shen, K. Dai, X. Zhang, H. Chen, Controllable synthesis of Bi 2 MoO 6 nanosheets and their facet-dependent visible-light-driven photocatalytic activity, Appl. Surf. Sci. 430 (2018) 505–514, https://doi.org/10.1016/j.apsusc.2017.08.072.
[11] H.L. Tan, X. Wen, R. Amal, Y.H. Ng, BiVO4 010 and 110 relative exposure extent: governing factor of surface charge population and photocatalytic activity, J. Phys. Chem. Lett. 7 (2016) 1400–1405, https://doi.org/10.1021/acs.jpclett.6b00428.
[12] X. Wu, Y.H. Ng, L. Wang, Y. Du, S.X. Dou, R. Amal, J. Scott, Improving the photo-oxidative capability of BiOBr: Via crystal facet engineering, J. Mater. Chem. A. 5 (2017) 8117–8124, https://doi.org/10.1039/c6ta10964k.
[13] T.-G. Vo, C.-C. Kao, J.-L. Kuo, C. Chiu, C.-Y. Chiang, Unveiling the crystallographic facet dependence of the photoelectrochemical glycerol oxidation on bismuth vanadate, Appl. Catal. B Environ. 278 (2020), 119303, https://doi.org/10.1016/j.apcatb.2020.119303.
[14] R. Kumar, A. Sudhaik, P. Raizada, A. Hosseini-Bandegharaei, V.K. Thakur, A. Saini, V. Saini, P. Singh, An overview on bismuth molybdate based photocatalytic systems: Controlled morphology and enhancement strategies for photocatalytic water purification, J. Environ. Chem. Eng. 8 (2020) 104291. https://doi.org/10.1016/j.jece.2020.104291.
[15] X. Yang, X. Xu, J. Wang, T. Chen, S. Wang, X. Ding, H. Chen, Insights into the surface/interface modifications of Bi 2 MoO 6: feasible strategies and photocatalytic applications, Sol. RRL. 5 (2021) 2000442, https://doi.org/10.1002/solr.202000442.
[16] J. Long, S. Wang, H. Chang, B. Zhao, B. Liu, Y. Zhou, W. Wei, X. Wang, L. Huang, W. Huang, Bi2MoO6 nanobelts for crystal facet-enhanced photocatalysis, Small. 10 (2014) 2791–2795, https://doi.org/10.1002/smll.201302950.
[17] X. Wu, Y.H. Ng, W.H. Saputera, X. Wen, Y. Du, S.X. Dou, R. Amal, J. Scott, The dependence of Bi 2 MoO 6 photocatalytic water oxidation capability on crystal facet engineering, ChemPhotoChem. 3 (2019) 1246–1253, https://doi.org/10.1002/cptc.201900113.
[18] M. Wu, Y. Wang, Y. Xu, J. Ming, M. Zhou, R. Xu, Q. Fu, Y. Lei, Self-supported Bi2MoO6 nanowall for photoelectrochemical water splitting, ACS Appl. Mater. Interfaces. 9 (2017) 23647–23653, https://doi.org/10.1021/acsami.7b03801.
[19] Y. Sun, H. Wang, Q. Xing, W. Cui, J. Li, S. Wu, L. Sun, The pivotal effects of oxygen vacancy on Bi2MoO6: promoted visible light photocatalytic activity and reaction mechanism, Chinese, J. Catal. 40 (2019) 647–655, https://doi.org/10.1016/S1872-2067(19)63277-8.

[20] Y. Ma, Z. Wang, Y. Jia, L. Wang, M. Yang, Y. Qi, Y. Bi, Bi2MoO6 nanosheet array modified with ultrathin graphitic carbon nitride for high photoelectrochemical performance, Carbon N. Y. 114 (2017) 591–600, https://doi.org/10.1016/j.carbon.2016.12.043.
[21] M. Zargazi, M.H. Entezari, Photoelectrochemical water splitting by a novel design of photo-anode: inverse opal-like UiO-66 sensitized by Pd and decorated with S, N graphene QDs, Electrochim. Acta. 391 (2021), 138926, https://doi.org/10.1016/j.electacta.2021.138926.
[22] S. Feng, T. Wang, B. Liu, C. Hu, L. Li, Z.J. Zhao, J. Gong, Enriched surface oxygen vacancies of photoanodes by photoetching with enhanced charge separation, Angew. Chemie - Int. Ed. 59 (2020) 2044–2048, https://doi.org/10.1002/anie.201913295.
[23] A. Landman, R. Halabi, P. Dias, H. Dotan, A. Mehlmann, G.E. Shter, M. Halabi, O. Naseraldeen, A. Mendes, G.S. Grader, A. Rothschild, Decoupled photoelectrochemical water splitting system for centralized hydrogen production, Joule. 4 (2020) 448–471, https://doi.org/10.1016/j.joule.2019.12.006.
[24] X. Shi, K. Zhang, K. Shin, M. Ma, J. Kwon, I.T. Choi, J.K. Kim, H.K. Kim, D.H. Wang, J.H. Park, Unassisted photoelectrochemical water splitting beyond 5.7% solar-to-hydrogen conversion efficiency by a wireless monolithic photoanode/dye-sensitised solar cell tandem device, Nano Energy. 13 (2015) 182–191, https://doi.org/10.1016/j.nanoen.2015.02.018.
[25] M.S. Prévot, K. Sivula, Photoelectrochemical tandem cells for solar water splitting, J. Phys. Chem. C. 117 (2013) 17879–17893, https://doi.org/10.1021/jp405291g.
[26] G. Li, W. Yang, S. Gao, Q. Shen, J. Xue, K. Chen, Q. Li, Creation of rich oxygen vacancies in bismuth molybdate nanosheets to boost the photocatalytic nitrogen fixation performance under visible light illumination, Chem. Eng. J. 404 (2021), 127115, https://doi.org/10.1016/j.cej.2020.127115.
[27] G. Yang, Y. Liang, K. Li, J. Yang, K. Wang, R. Xu, X. Xie, Engineering the dimension and crystal structure of bismuth molybdate photocatalysts via a molten salt-assisted assembly approach, J. Alloys Compd. 844 (2020), 156231, https://doi.org/10.1016/j.jallcom.2020.156231.
[28] W. Dai, J. Long, L. Yang, S. Zhang, Y. Xu, X. Luo, J. Zou, S. Luo, Oxygen migration triggering molybdenum exposure in oxygen vacancy-rich ultra-thin Bi2MoO6 nanoflakes: Dual binding sites governing selective CO2 reduction into liquid hydrocarbons, J. Energy Chem. 61 (2021) 281–289, https://doi.org/10.1016/j.jechem.2021.01.009.
[29] X. Xu, X. Ding, X. Yang, P. Wang, S. Li, Z. Lu, H. Chen, Oxygen vacancy boosted photocatalytic decomposition of ciprofloxacin over Bi2MoO6: Oxygen vacancy engineering, biotoxicity evaluation and mechanism study, J. Hazard. Mater. 364 (2019) 691–699, https://doi.org/10.1016/j.jhazmat.2018.10.063.
[30] C. Chen, G. Qiu, T. Wang, Z. Zheng, M. Huang, B. Li, Modulating oxygen vacancies on bismuth-molybdate hierarchical hollow microspheres for photocatalytic selective alcohol oxidation with hydrogen peroxide production, J. Colloid Interface Sci. 592 (2021) 1–12, https://doi.org/10.1016/j.jcis.2021.02.036.
[31] J. Long, S. Wang, H. Chang, B. Zhao, B. Liu, Y. Zhou, W. Wei, X. Wang, L. Huang, W. Huang, Bi 2 MoO 6 nanobelts for crystal facet-enhanced photocatalysis, Small. 10 (2014) 2791–2795, https://doi.org/10.1002/smll.201302950.
[32] K. Ye, K. Li, Y. Lu, Z. Guo, N. Ni, H. Liu, Y. Huang, H. Ji, P. Wang, An overview of advanced methods for the characterization of oxygen vacancies in materials, TrAC Trends Anal. Chem. 116 (2019) 102–108, https://doi.org/10.1016/j.trac.2019.05.002.
[33] Y. Wang, J. Zhang, M.-S. Balogun, Y. Tong, Y. Huang, Oxygen vacancy–based metal oxides photoanodes in photoelectrochemical water splitting, Mater. Today Sustain. 18 (2022), 100118, https://doi.org/10.1016/j.mtsust.2022.100118.
[34] X. Yang, S. Wang, N. Yang, W. Zhou, P. Wang, K. Jiang, S. Li, H. Song, X. Ding, H. Chen, J. Ye, Oxygen vacancies induced special CO2 adsorption modes on Bi2MoO6 for highly selective conversion to CH4, Appl. Catal. B Environ. 259 (2019), 118088, https://doi.org/10.1016/j.apcatb.2019.118088.
[35] Y. Wang, D. Chen, J. Zhang, M.S. Balogun, P. Wang, Y. Tong, Y. Huang, Charge relays via dual carbon-actions on nanostructured BiVO4 for high performance photoelectrochemical water splitting, Adv. Funct. Mater. 32 (2022) 1–9, https://doi.org/10.1002/adfm.202112738.
[36] F. Yang, T. Xiong, P. Huang, S. Zhou, Q. Tan, H. Yang, Y. Huang, M.-S. Jie T. Balogun, Nanostructured transition metal compounds coated 3D porous core-shell carbon fiber as monolith water splitting electrocatalysts: a general strategy, Chem. Eng. J. 423 (2021), 130279, https://doi.org/10.1016/j.cej.2021.130279.
[37] B. Klahr, S. Gimenez, F. Fabregat-Santiago, J. Bisquert, T.W. Hamann, Electrochemical and photoelectrochemical investigation of water oxidation with hematite electrodes, Energy Environ. Sci. 5 (2012) 7626, https://doi.org/10.1039/c2ee21414h.
[38] P. Tang, H. Xie, C. Ros, L. Han, M. Biset-Peiró, Y. He, W. Kramer, A.P. Rodríguez, E. Saucedo, J.R. Galán-Mascarós, T. Andreu, J.R. Morante, J. Arbiol, Enhanced photoelectrochemical water splitting of hematite multilayer nanowire photoanodes by tuning the surface state via bottom-up interfacial engineering, Energy Environ. Sci. 10 (2017) 2124–2136, https://doi.org/10.1039/C7EE01475A.
[39] J. Fu, Z. Fan, M. Nakabayashi, H. Ju, N. Pastukhova, Y. Xiao, C. Feng, N. Shibata, K. Domen, Y. Li, Interface engineering of Ta3N5 thin film photoanode for highly efficient photoelectrochemical water splitting, Nat. Commun. 13 (2022) 729, https://doi.org/10.1038/s41467-022-28415-4.
[40] H. Wang, Y. Xia, H. Li, X. Wang, Y. Yu, X. Jiao, D. Chen, Highly active deficient ternary sulfide photoanode for photoelectrochemical water splitting, Nat. Commun. 11 (2020) 3078, https://doi.org/10.1038/s41467-020-16800-w.
[41] R. Chen, S. Pang, H. An, T. Dittrich, F. Fan, C. Li, Giant defect-induced effects on nanoscale charge separation in semiconductor photocatalysts, Nano Lett. 19 (2019) 426–432, https://doi.org/10.1021/acs.nanolett.8b04245.